Engineering 17 (2022) 183–195

Contents lists available at ScienceDirect

Engineering

journal homepage: www.elsevier.com/locate/eng

Research
Medical Additive Manufacturing—Article

3D-Printed Scaffolds Promote Angiogenesis by Recruiting Antigen-Specific T Cells

Cuidi Li [a,#], Zhenjiang Ma [b,#], Wentao Li [b], Tianyang Jie [a], Liping Zhong [c], Hongfang Chen [b], Wenhao Wang [b], Jinwu Wang [b,*], Wenguo Cui [a,*], Yongxiang Zhao [c,*]

[a] *Department of Orthopaedics, Shanghai Key Laboratory for Prevention and Treatment of Bone and Joint Diseases, Shanghai Institute of Traumatology and Orthopaedics, Ruijin Hospital, Shanghai Jiao Tong University School of Medicine, Shanghai 200025, China*
[b] *Department of Orthopedic Surgery, Shanghai Key Laboratory of Orthopedic Implants, Shanghai Ninth People's Hospital, Shanghai Jiao Tong University School of Medicine, Shanghai 200011, China*
[c] *National Center for International Research of Bio-targeting Theranostics, Guangxi Key Laboratory of Bio-targeting Theranostics, Collaborative Innovation Center for Targeting Tumor Theranostics, Guangxi Medical University, Nanning 530021, China*

ARTICLE INFO

Article history:
Received 1 April 2021
Revised 25 May 2021
Accepted 30 May 2021
Available online 17 August 2021

Keywords:
3D printing
Immune microenvironment regulating
Angiogenesis
Bone regeneration

ABSTRACT

The immune response after implantation is a primary determinant of the tissue-repair effects of three-dimensional (3D)-printed scaffolds. Thus, scaffolds that can subtly regulate immune responses may display extraordinary functions. Inspired by the angiogenesis promotion effect of humoral immune response, we covalently combined mesoporous silica microrod (MSR)/polyethyleneimine (PEI)/ovalbumin (OVA) self-assembled vaccines with 3D-printed calcium phosphate cement (CPC) scaffolds for local antigen-specific immune response activation. With the response activated, antigen-specific $CD4^+$ T helper 2 (Th2) cells can be recruited to promote early angiogenesis. The silicon (Si) ions from MSRs can accelerate osteogenesis, with an adequate blood supply being provided. At room temperature, scaffolds with uniformly interconnected macropores were printed using a self-setting CPC-based printing paste, which promoted the uniform dispersion and structural preservation of functional polysaccharides oxidized hyaluronic acid (OHA) inside. Sustained release of OVA was achieved with MSR/PEI covalently attached to scaffolds rich in aldehyde groups as the vaccine carrier. The vaccine-loaded scaffolds effectively recruited and activated dendritic cells (DCs) for antigen presentation and promoted the osteogenic differentiation of bone marrow mesenchymal stem cells (BMSCs) *in vitro*. When embedded subcutaneously *in vivo*, the vaccine-loaded scaffolds increased the proportion of Th2 cells in the spleen and locally recruited antigen-specific T cells to promote angiogenesis in and around the scaffold. Furthermore, the result in a rat skull defect-repair model indicated that the antigen-specific vaccine-loaded scaffolds promoted the regeneration of vascularized bone. This method may provide a novel concept for patient-specific implant design for angiogenesis promotion.

1. Introduction

Large bone defects caused by trauma and disease vary in shape and rarely self-heal; thus, bone-repair implants that meet individual needs are in great demand. However, the number of autogenous and allogeneic bones commonly used in clinics is limited [1]. As a manufacturing technique, three-dimensional (3D) printing can be used to prepare bone-repair implants with personalized shapes and inner structures, thanks to the diversity of applicable materials and designability of structures [2–6], which are ideal for clinical application. 3D-printed implants have been used clinically and have exhibited tissue-repair properties. Their well-interconnected pore structures have been verified to be suitable for tissue ingrowth and to promote osteointegration [7]. Nevertheless, angiogenesis promotion in large implants remains challenging. The autogenous vascular networks are often destroyed in large bone defects. Poor angiogenesis in the implants may lead to a lack of the nutrients and oxygen needed for cell growth in the implants, ultimately causing necrosis of the central site and failure of bone repair [8,9]. Angiogenesis promotion is a major requirement that should be met by implants before their extensive clinical application. In

* Corresponding authors.
E-mail addresses: wangjw@shsmu.edu.cn (J. Wang), wgcui80@hotmail.com (W. Cui), yongxiang_zhao@126.com (Y. Zhao).
[#] These authors contributed equally to this work.

https://doi.org/10.1016/j.eng.2021.05.018

addition, local blood flow and the amount of nutrient delivery are closely linked to the rate of bone regeneration [10,11]. Accelerated angiogenesis in printed implants is expected to provide sufficient nutrients for bone reconstruction, thus facilitating tissue repair. Traditional methods promote angiogenesis by directly incorporating growth factors—such as fibroblast growth factor (FGF) and vascular endothelial growth factor (VEGF)—into bone-repair materials [12,13]. At present, angiogenesis failure caused by the short half-life period and swift loss of growth factors can be partially overcome by designing materials with sustained release functions. However, a single growth factor is insufficient to promote the formation of mature blood vessels. More importantly, the number and activity of local immune cells around bone-repair implants are major determinants of angiogenesis properties [14,15]. Therefore, it is a worthwhile research direction to develop 3D-printed bone-repair implants with improved angiogenic properties by regulating the local immune microenvironment.

Recently, functional growth factors and biomaterials with mononuclear cell-/macrophage-regulating properties have been introduced into 3D-printed scaffolds to promote angiogenesis and bone repair [16–19]. Macrophages play an important role in angiogenesis [20,21]. It has been demonstrated that M1 macrophages promote angiogenesis initiation, whereas M2 macrophages enhance vascular maturation and remodeling [22,23]. 3D-printed scaffolds that sequentially release interferon-γ (IFN-γ) and silicon (Si) ions have been designed to polarize macrophages first to M1 and then to M2 phenotypes [16]. Enhanced angiogenesis was observed in these scaffolds in a subcutaneous embedding model. However, macrophage activation shows a continuous state according to external stimuli, with M1 and M2 types representing two extremes [24,25]. Importantly, polarization is not completely controllable within a complex tissue microenvironment *in vivo*. In addition, macrophages exert regulatory effects on the functions of osteogenesis, osteolysis, angiogenesis, and so forth, whereas the respective mechanisms are different [22,26–28]. Inappropriate regulation could therefore lead to tissue damage. Thus, the precise regulatory mechanisms of macrophage polarization to promote vascularized bone tissue reconstruction by 3D-printed scaffolds are relatively complex.

Notably, 3D-printed scaffolds with T cell regulatory functions also have the potential to promote angiogenesis and bone regeneration. The T cell-associated adaptive immune system plays a crucial role in the repair of bone defects and promotion of angiogenesis [29–33]. Although T cells, like macrophages, have many subtypes, the conditioned medium of $CD4^+$ T cells significantly promotes the osteogenic mineralization of human mesenchymal stem cells [31]. In addition, $CD4^+$ T cells have been found to promote arterial formation in hindlimb ischemia models [32,33]. In particular, $CD4^+$ T helper 2 (Th2) cells not only secrete growth factors that contribute to angiogenesis during ischemic injury [34], but also activate eosinophils to secrete related growth factors [35]. Therefore, 3D-printed scaffolds have the capability to locally recruit and activate Th2 cells, which may promote both angiogenesis and osteogenesis at defect sites. Kwee et al. [36] implanted nano-aluminum/ovalbumin (OVA) vaccines into an ischemic hindlimb model and verified that the released OVA antigen could specifically recruit Th2 cells, trigger local angiogenesis, increase blood perfusion in ischemic limbs, and reduce muscle necrosis. Aluminum nanoparticles are a traditional vaccine vector and immune adjuvant that promotes the recruitment and activation of Th2 cells by OVA. However, nanoparticle vaccines would rapidly disperse into the systemic circulation after being injected into a bone defect, and are thus unlikely to achieve the aim of recruiting local cells. In addition, a vaccine–nanoparticle system alone is unsuitable for bone-defect repair. Therefore, with specific vectors and relevant combination methods designed according to the specific requirements of the bone defect, OVA vaccine-loaded 3D-printed scaffolds might promote angiogenesis and bone regeneration by locally releasing OVA and recruiting antigen-specific T cells.

Previously, we introduced mesoporous silica microrods (MSRs) into self-setting calcium phosphate cement (CPC) paste as a bioink and successfully 3D printed personalized bone-repair scaffolds [37]. The Si ions released from the scaffolds effectively promoted bone formation. In this study, inspired by the angiogenesis-regulating function of T cells, Th2 cell-specific vaccines were prepared by assembling MSRs, branched polyethyleneimine (PEI), and OVA layer by layer through a simple adsorption approach, and then covalently combining these vaccines with printed calcium phosphate bone-repair scaffolds based on a Schiff base reaction to construct 3D-printed bone-repair scaffolds that locally recruited Th2 cells and promoted angiogenesis (Fig. 1). With the MSRs as a vector, the OVA/MSR vaccine was capable of activating specific Th2 cell responses [38]. With coating of the cationic polymer PEI, MSR/PEI microrods (referred to herein as MSR/PEIs) further promoted the activation of dendritic cells (DCs) and enhanced T cell responses as the OVA vaccine vector [39]. The introduction of oxidized hyaluronic acid (OHA) into the calcium phosphate printing inks rendered the scaffolds rich in aldehyde groups and allowed them to swiftly crosslink with MSR/PEI/OVA vaccines (herein referred to as MSR/PEI/OVAs) full of amidogen, thus promoting the stable combination of vaccines and scaffolds. The gradually released OVA resulted in the recruitment of Th2 cells, which secrete angiogenic-related growth factors and promote angiogenesis. *In vitro* results showed that releasing OVA from the scaffolds rapidly recruited and activated DCs for antigen presentation. Moreover, the released Si ions effectively promoted the osteogenic differentiation of bone marrow mesenchymal stem cells (BMSCs). In the subcutaneous embedding model, the vaccine-loaded scaffolds rapidly activated and recruited Th2 cells at the early stage of implantation and significantly promoted the formation of local blood vessels. In the *in situ* skull defect-repair model, vaccine-loaded 3D-printed scaffolds promoted both angiogenesis and osteogenesis.

2. Materials and methods

2.1. Vaccine formulations

MSRs were synthesized via the sol–gel method, as described previously [37], with tetraethylorthosilicate (Sinopharm Chemical Reagent, China) being used as a silica source. To formulate the MSR/PEI vaccine vector, 40 μL of the MSR working solution (50 $mg \cdot mL^{-1}$ in phosphate buffer solution (PBS)) was mixed with 100 μL of branched PEI solution (25 $\mu g \cdot mL^{-1}$ in PBS) at 37 °C for 15 min. Subsequently, 100 μg of OVA was incubated with MSR/PEIs at 37 °C for 1 h in an oscillating incubator to obtain MSR/PEI/OVAs. The microrods were freeze dried for further physical analysis. The morphology of the MSRs and MSR/PEI was analyzed via scanning electron microscopy (SEM; TESCAN, USA). The mesoporous structures of the MSRs and MSR/PEIs were assessed using a specific surface and porosity analyzer (Quantachrome, USA) and transmission electron microscopy (TEM; FEI, Japan). MSR/PEIs were assayed with energy dispersive spectroscopy (EDS; TESCAN) to analyze the incorporation capacity of PEI and MSRs. The zeta potentials of the microrods were analyzed using a nanoscale zeta potentiometer (Omni, USA).

2.2. Vaccine loading on scaffolds

OHA was synthesized via a slightly modified procedure [39]. Fourier-transform infrared (FTIR) spectra of the hyaluronic acid

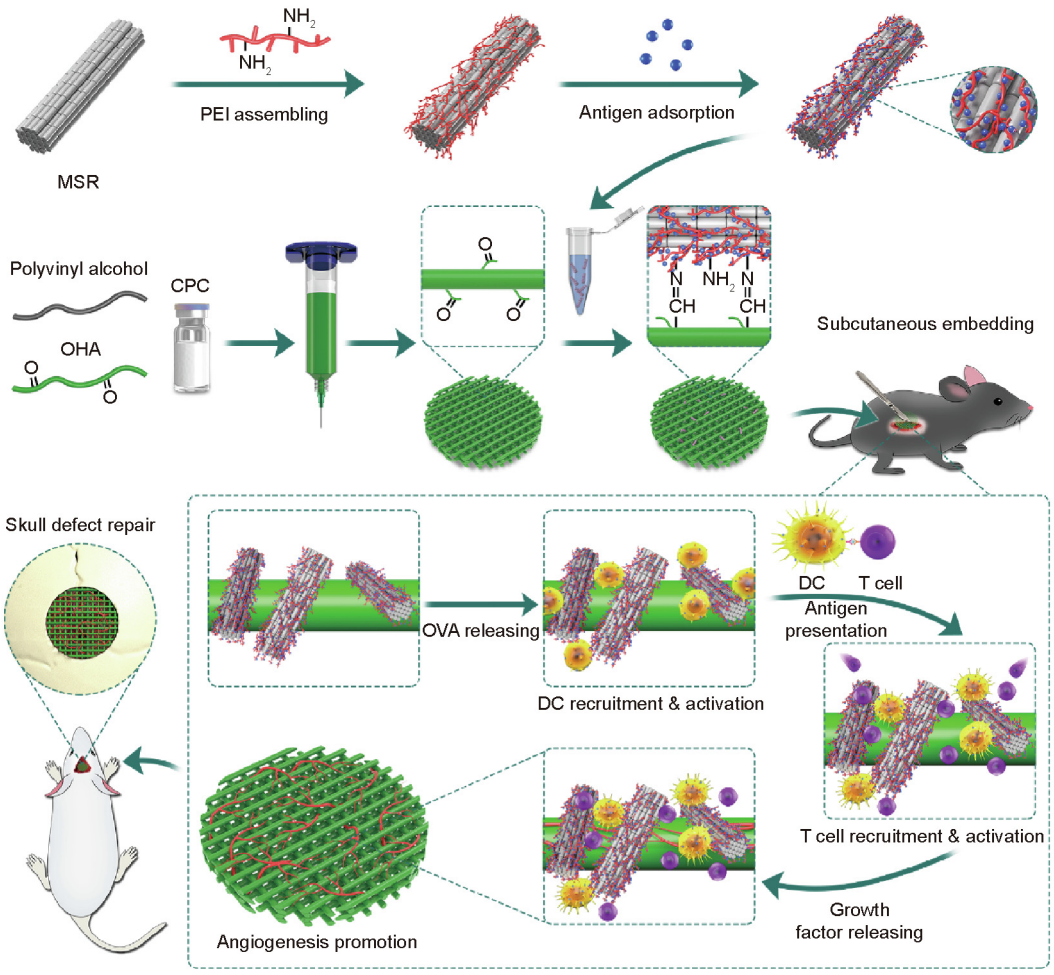

Fig. 1. Schematic illustration of the construction, local humoral immune responses activation, and angiogenesis promotion of the vaccine-loaded 3D-printed scaffold. MSR/PEI/OVA self-assembled vaccines were covalently combined on 3D-printed CPC scaffolds rich in aldehyde groups, allowing the humoral immune response to be locally activated through the gradual release of OVA. With the response activated, antigen-specific $CD4^+$ T cells were recruited to promote early angiogenesis. OHA: oxidized hyaluronic acid; DC: dendritic cell.

(HA) and OHA were assessed using an FTIR spectrometer (Thermo Scientific Co., USA).

Subsequently, 1 wt% OHA aqueous solution was gently mixed with 10 wt% polyvinyl alcohol (M_w = 98 000; Sigma-Aldrich, USA) aqueous solution to form a setting solution that was rich in aldehyde groups. By evenly mixing CPC powder (Rebone, China) with the setting solution, a printable paste was prepared, which was fed into a printing syringe (Cellink, Sweden) and then printed at room temperature. The printed scaffolds were hydrated overnight in a 100% humidity chamber at 37 °C and then air dried.

Next, 1 and 2 mg of MSR/PEI/OVA microrods were resuspended in PBS and deposited onto the printed CPC scaffolds to form the vaccine-loaded scaffolds (CPC-MSR/PEI/OVA) for *in vitro* and *in vivo* experiments, respectively. MSR/PEI-loaded scaffolds were prepared with the same procedure and were used as the vaccine vector-loaded scaffold (CPC-MSR/PEI) group.

2.3. OVA release from scaffolds

To determine OVA release from the scaffolds, each of the CPC-MSR/PEI/OVA scaffolds (sized 10 mm × 10 mm × 2 mm) was placed in 1 mL of PBS and co-incubated at 37 °C. At various time-points, the supernatant was completely collected and replaced with fresh PBS. The concentration of OVA in the supernatant was assayed using a Pierce Micro-BCA protein assay kit (Thermo Fisher Scientific). The amount of released OVA was calculated for release curve plotting.

2.4. Si ion release from scaffolds

To determine Si ion release from the scaffolds, each of the scaffolds (sized 10 mm × 10 mm × 2 mm) was placed in 1 mL of PBS and incubated at 37 °C. The supernatant was completely collected and replaced with fresh PBS every other day. The concentration of Si ions in the supernatant was assayed using an inductive coupled plasma emission spectrometer (Thermo Fisher Scientific).

2.5. DC differentiation, activation, and antigen presentation assays

For DC differentiation, activation, and antigen presentation assays, DCs were inducing cultured from the bone marrow cells of C57BL/6J mice (Jihui Laboratory Animal Co., Ltd., China) with

Roswell Park Memorial Institute (RPMI) medium (Thermo Fisher Scientific) supplemented with 10% fetal bovine serum (Thermo Fisher Scientific), 1% penicillin/streptomycin, and 20 ng·mL^{-1} murine granulocyte–macrophage colony-stimulating factor (PeproTech, USA), as previously described [36]. After 8 days of inducing culture, non-adherent cells were collected for the experiments. To assess the DCs' activity after co-culture with the scaffolds, 1×10^6 mL^{-1} immature DCs were seeded onto the scaffolds in 12-well plates and co-cultured for 24 h. Afterward, the DCs were harvested, stained with anti-CD11c, anti-CD86, and anti-major histocompatibility complex class II (MHC II) (Biolegend, USA), and analyzed via LSRFortessa flow cytometry (BD, USA). Cells attaching onto the scaffolds were stained using anti-MHC II for surface markers and diaminophenylindane (DAPI) for the nuclei; subsequently, they were observed using a confocal microscope (Zeiss, Germany).

To assess the cross-presentation of DCs after stimulation, 5×10^5 mL^{-1} DCs were seeded onto the scaffolds and co-cultured for 48 h. The DCs in the supernatant were harvested and stained using anti-SIINFEKL-H2K^b and analyzed via flow cytometry. The DCs in the scaffolds were stained using anti-SIINFEKL-H2K^b for surface markers and DAPI for the nuclei; subsequently, they were observed using a confocal microscope.

2.6. Cells and scaffold extraction preparation for osteogenic assays

Cells and scaffolds were prepared for osteogenic assays as follows. Mice BMSCs (mBMSCs) were isolated from C57BL/6J mice and cultured as previously described [40]. CPC, CPC-MSR/PEI, and CPC-MSR/PEI/OVA scaffolds (sized 10 mm × 10 mm × 2 mm) were prepared as described. Each scaffold was placed into a 24-well culture plate and immersed in 1 mL of alpha-minimum essential medium (Thermo Fisher Scientific). The medium was replaced every other day. After 7 days of immersion, the scaffolds were lyophilized and collected for further use. The extractions of CPC, CPC-MSR/PEI, and CPC-MSR/PEI/OVA scaffolds were prepared and stored at 4 °C, as previously described [37].

2.7. Cell attachment

To determine cell attachment, a total of 5×10^4 mBMSCs were seeded onto each of the scaffolds in 24-well plates and cultured for 24 h. Next, the scaffolds were fixed with 4% paraformaldehyde (PFA). The cell attachment on the scaffolds was assayed via SEM after gradient elution and natural drying.

2.8. Alkaline phosphatase activity assay

For the alkaline phosphatase (ALP) activity assay, a total of 5×10^4 mBMSCs were seeded onto each of the scaffolds in 24-well plates. The culture medium was replaced every 3 days. After 7 days of culture, the cells were fixed with 4% PFA, stained using an ALP kit (Beyotime, China), and observed using optical microscopy (Nikon, Japan).

2.9. Cell viability

To determine cell viability, a total of 1×10^4 mBMSCs were seeded onto each of the scaffolds in 24-well plates and cultured for 12 h. Next, the culture medium was replaced with extractions of the processed scaffolds. After 1 and 3 days of culture, the cell viability was assayed using a cell counting kit-8 (CCK-8; Solarbio, China). Cells in standard culture medium without replacement were set as the control group.

2.10. Real-time quantitative polymerase chain reaction

For the real-time quantitative polymerase chain reaction (PCR) assay, mBMSCs were seeded into 6-well plates at a density of 5×10^4 per well and allowed to grow until they covered the well. Afterward, the culture medium was replaced with the prepared extractions of scaffolds. The extraction medium was replaced every 3 days. After 14 days of culture, the cells were washed with PBS, and the total messenger RNA (mRNA) was extracted and converted to complementary DNA. The expression of osteogenesis-related genes including *ALP* and runt-related transcription factor 2 (*RUNX2*) was assayed through a real-time quantitative PCR assay. The relative amount of gene transcripts was normalized to glyceraldehyde-3-phosphate dehydrogenase (GAPDH). The primers are listed in Table S1 in Appendix A.

2.11. Subcutaneous implantation model

For the *in vivo* immunoregulation and vascularization study, each of the CPC, CPC-MSR/PEI, and CPC-MSR/PEI/OVA scaffolds (diameter = 6 mm; height = 2 mm) was implanted in a subcutaneous pocket prepared via blunt dissection (number of parallel samples per group, $n = 6$). Mice that underwent sham surgery were set as the control group ($n = 6$). The C57BL/6J mice (6 weeks old) used in this study were obtained from Shanghai Jihui Laboratory Animal Co., Ltd. The animal experiments were performed in accordance with the guidelines and regulations of the Institutional Animal Care and Use Committee of Ruijin Hospital, Shanghai Jiao Tong University School of Medicine.

2.11.1. *T cell activation and recruitment* in vivo

T cell activation and recruitment *in vivo* were determined as follows. After 7 days of implantation, the animals were sacrificed and the scaffolds were collected. The splenocytes were meticulously isolated from the spleen, and then processed and cultured for 1 day at 37 °C. Afterward, the cells were collected and stained with anti-mouse CD3e, CD8a, and CD4 (Biolegend) on ice before they were fixed and permeabilized. Next, the cells were stained with anti-mouse interleukin (IL)-4 and IFN-γ at 4 °C and analyzed using flow cytometry.

The retrieved scaffolds were decalcified, embedded in paraffin, and sectioned. The sections were deparaffinized, rehydrated, and then incubated separately with primary antibody against CD4 and CD31 (Abcam, USA) overnight at 4 °C. After being stained with a secondary antibody and DAPI, sections were observed via confocal microscope to evaluate the local immunoregulatory function of the scaffolds. The mean fluorescence intensity was calculated using Image J software (Softonic, Spain) to evaluate the recruited cells.

2.11.2. In vivo *angiogenesis*

In vivo angiogenesis was determined as follows. After 14 days of implantation, local blood stream signals in and around the scaffolds were assayed using a multimode ultrasound/photoacoustic imaging system VEVO LAZR-X (Fujifilm VisualSonics Inc., Canada) to analyze the newly formed blood vessels in each group. Subsequently, the mice were sacrificed, and the scaffolds were collected for immunohistochemistry assay. The samples were decalcified, embedded in paraffin, and sectioned. The sections were deparaffinized, rehydrated, and then incubated separately with a primary antibody against CD31 overnight at 4 °C. After being stained with a secondary antibody and DAPI, sections were observed via confocal microscope. The mean fluorescence intensity was calculated using Image J software to evaluate the degree of angiogenesis.

2.12. In situ *defect-repair model*

To analyze the *in vivo* osteogenesis property of the scaffolds, a calvarial defect-repair model was established based on a previous study [41]. A total of 24 healthy male Sprague Dawley (SD) rats (8 weeks old) were divided into four groups: ① untreated, ② CPC, ③ CPC-MSR/PEI, and ④ CPC-MSR/PEI/OVA. A 4 mm-diameter defect was created for each rat using a trephine bur. The incision was closed after the scaffold (diameter = 4 mm; height = 1.5 mm) was implanted. After 8 weeks of implantation, the skulls were collected and fixed in 4% PFA for further analysis (n = 6).

2.13. Micro-computerized tomography analysis

All samples were scanned with a resolution of 20 μm for the bone formation assay using a micro-computed tomography (CT) imaging system (Bruker, Germany). Subsequently, the scanning results were reconstructed three-dimensionally using DataViewer software (SR Research, Canada). The scaffold and bone were reconstructed separately based on their different gray value ranges (scaffold (175–255); bone (120–174)). To distinguish observations, the scaffolds and newly formed bone were rendered in yellow and white, respectively. The volume ratio of the newly formed bones was calculated.

2.14. Histology evaluation

For histology evaluation, after fixation with 4% PFA, the samples were decalcified, embedded in paraffin, and sectioned. The sections were stained with hematoxylin/eosin (HE) and Masson's trichrome and observed via optical microscopy TE2000U (Nikon). In Masson's trichrome-stained sections, typical bone tissues displaying red color were regarded as the mature ones. Furthermore, immunohistochemistry staining against CD31 was performed to assay the newly formed vascular structure in the scaffolds, as previously described [40].

2.15. Statistical analysis

For statistical analysis, the data were presented as mean ± standard deviation. Statistically significant differences among the various groups were measured via one-way analysis of variance (ANOVA) using the GraphPad Prism 5 software package (GraphPad Software, USA).

3. Results and discussion

3.1. Scaffolds loaded with vaccines

To fabricate the vaccine-loaded scaffolds, self-assembling vaccines were first prepared and assessed. The MSRs were mixed with the branched PEI solution and incubated at 37 °C for 15 min to form PEI-coated MSR/PEIs. Typical lamellar mesopores were observed in MSRs and MSR/PEIs using TEM (Fig. 2(a)). According to the specific surface and porosity assay results (Fig. 2(a)), both MSRs and MSR/PEIs displayed type IV N_2 adsorption/desorption isotherms with the H1 hysteresis loop, which verified the ordered mesoporous structure. The pore size, total pore volume, and specific surface area of MSRs were 7.8 nm, 1.25 $cm^3 \cdot g^{-1}$, and 849.9 $m^2 \cdot g^{-1}$, respectively. As previously reported [42], MSR/PEIs had a maintained pore size (7.8 nm) and a slightly decreased pore volume and specific surface area, which were 0.973 $cm^3 \cdot g^{-1}$ and 618.9 $m^2 \cdot g^{-1}$, respectively. It was presumed that the coating of PEI on the mesopores of the rod surface resulted in this decrease. According to the SEM assay results, prismatic nanorods measuring 600 nm accumulated and formed the MSRs, which had a length of around 23.2 μm and a diameter of around 3.7 μm (Fig. 2(b)). No obvious change in outer shape was detected in MSR/PEIs. We analyzed the distribution of the nitrogen (N) element of PEI on the MSRs and the distribution of the oxygen (O) and Si elements of the MSRs in the EDS mapping images in order to observe the incorporation capacity of PEI and MSRs. The similar distributions of the N, O, and Si elements verified the presence of a sufficient and even coating of PEI on the MSRs (Fig. 2(c)). Due to the high pore volume, high specific surface area, and positive charges, the MSR/PEIs could be used as the vector of antigens to achieve sustained release. In this study, OVA was used as an antigen model. MSR/PEIs were dispersed in an OVA antigen solution for direct adsorption. The zeta potentials of the MSRs, MSR/PEIs, and MSR/PEI/OVA microrods were (−22.33 ± 1.80), (29.50 ± 0.46), and (19.47 ± 1.70) mV, respectively (Fig. 2(d)), which confirmed the successful self-assembling of the vaccines (Fig. 2(e)). After PBS dispersion, Si hydroxyl on the surface of the MSRs provided them with a negative zeta potential. With good coating of the polycation PEI, the zeta potential of the MSR/PEIs changed from negative (MSRs) to positive. The incorporation of OVA, a peptide with a negative charge, rendered the zeta potential of the MSR/PEI/OVAs lower than that of the MSR/PEIs.

Afterward, the vaccine-loaded scaffolds were prepared and assayed. According to the FTIR results (Fig. 3(a)), a new absorption peak at approximately 1715.3 cm^{-1} corresponding to the aldehyde groups appeared in the spectrum of OHA, which verified our successful synthesis. With PVA/OHA solution as the binder, the CPC-based bioink could be fluently extruded from the printing nozzle. SEM observation showed that the printed CPC scaffolds possessed controllable shapes and well-interconnected macropores measuring 500 μm. In addition, the MSR/PEIs were seen to be dispersed well on the scaffolds (Fig. 3(b)). To avoid having the vaccines be carried away rapidly by blood, the vaccines were designed to combine with the printed scaffolds via covalent bonding. Hence, we analyzed the antigen and Si ion releasing behavior of the scaffolds. According to the protein assay results (Fig. 3(c)), OVA was gradually released from the scaffolds over 7 days, with a burst release in the first 24 h. It was discovered that the Si ion concentration in the releasing medium decreased gradually from 6 to 1 $mg \cdot L^{-1}$ in 72 h and was then maintained at approximately 1 $mg \cdot L^{-1}$, with the medium being replaced daily (Fig. 3(d)); this verified the relatively stable combination between the MSR/PEIs and CPC scaffolds.

3.2. Vaccine-loaded scaffolds recruit and activate DCs

The activation of a large number of DCs is closely associated with the induction effect of humoral immune responses [43,44]. Hence, the MSR/PEI/OVA-loaded scaffolds were analyzed for their ability to modulate the enrichment, activation, and antigen processing of DCs as vaccines. First, cell recruitment to the vaccine-loaded scaffolds was analyzed. As observed via SEM, the cells were recruited to the vectors and vaccine-loaded scaffolds in 24 h and attached primarily on the microrods, whereas only a few of them were observed in the CPC scaffolds (Fig. 4(a)). Subsequently, the expression levels of two typical markers—namely, CD86 and MHC II—were analyzed in order to assess the activation of DCs based on previous reports [45,46]. The confocal microscope results (Fig. 4(a)) showed that the MHC II^+ recruited cells spread on the surfaces of the MSR/PEIs and MSR/PEI/OVAs, and exhibited the specific microrod morphology. Furthermore, the flow cytometry results (Fig. 4(b)) of the cell composition in the culture medium showed that the $CD11c^+$ DCs displayed 28.7%, 36.7%, and 39.4% $CD86^+$, and 31.6%, 38.7%, and 41.0% MHC II^+ in the CPC, CPC-MSR/PEI, and CPC-MSR/PEI/OVA groups, respectively. After 48 h of culture, the effects of the vaccine-loaded scaffolds on the antigen

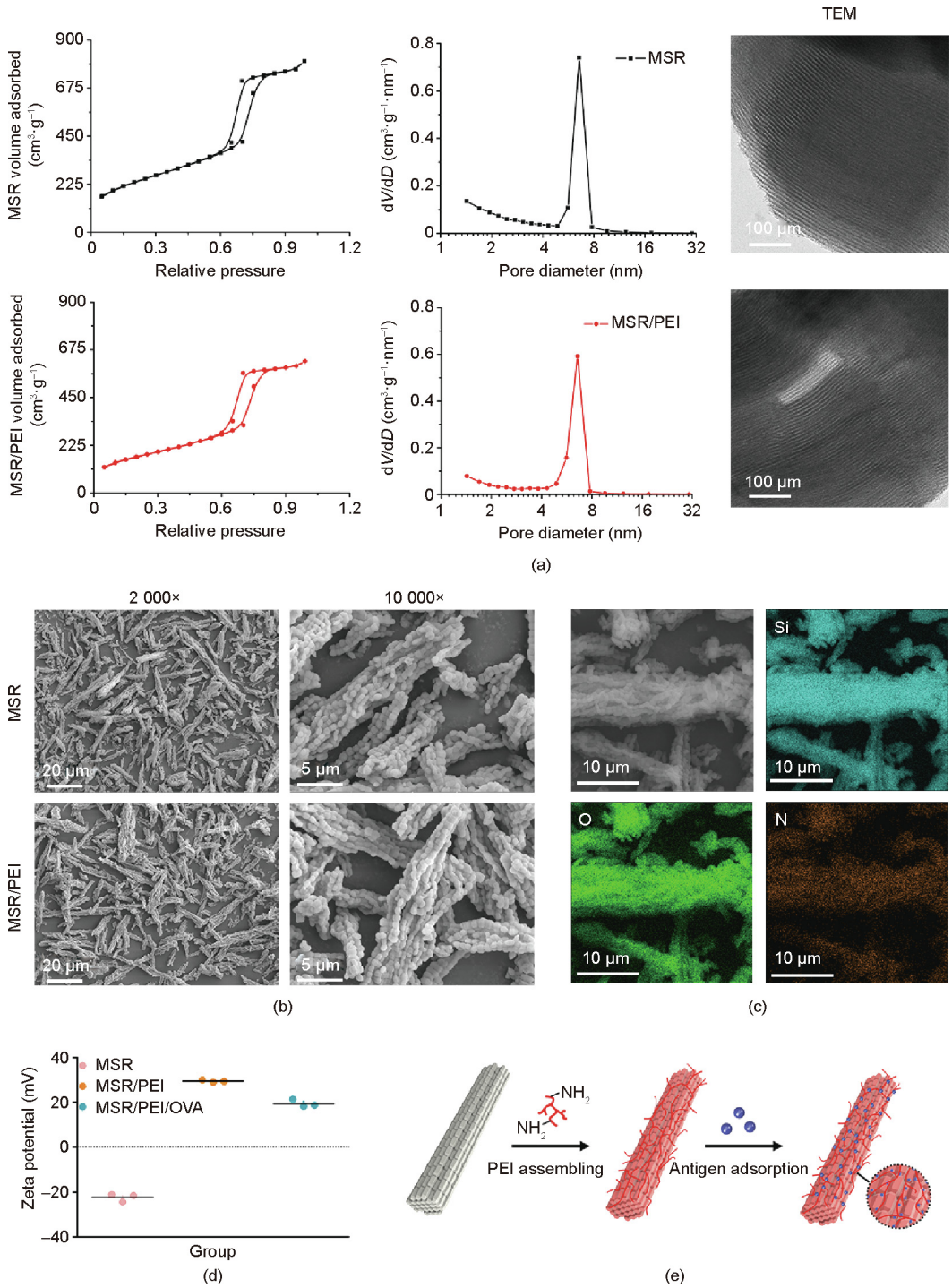

Fig. 2. Preparation and characterization of the MSR vaccine. (a) N_2 adsorption/desorption isotherms, pore size distribution, and TEM images of MSRs and MSR/PEIs. (b) SEM images of MSRs and MSR/PEIs. (c) EDS mapping images of MSR/PEIs. (d) Zeta potentials of MSRs, MSR/PEIs, and MSR/PEI/OVAs. (e) Schematic representations of the branched PEI and subsequent antigen adsorption onto MSRs. *V*: pore volume; *D*: pore diameter.

presentation of the DCs were analyzed. Under a microscope, DCs were seen to be recruited to the released MSR/PEIs and MSR/PEI/OVAs in the macropores of the scaffolds and aggregated (Fig. 4(c)). In addition, using a confocal microscope, more SIINFEKL-H2K^{b+} antigen cross-presenting DCs were observed on the CPC-MSR/PEI/OVA scaffolds than on the CPC-MSR/PEI and CPC scaffolds (Fig. 4(d)). Furthermore, the cells in the culture medium were assayed via flow cytometry analysis (Fig. 4(e)). It was revealed that the proportion of CD11c^{+} DCs displaying SIINFEKL-H2K^{b+} was 10.5%, 12.4%, and 15.0% in the CPC, CPC-MSR/PEI, and CPC-MSR/PEI/OVA groups, respectively. As a potential biocompatible vaccine adjuvant, MSRs are able to enhance the expression of CD86 after being co-cultured with human DCs [47]. Herein, the loading of MSR/PEIs on the 3D-printed scaffolds was found to not only activate the DCs, but also promote the antigen process. Furthermore, the efficient DC activation function of the MSR/PEI/OVA-loaded scaffolds was confirmed, with the largest number of recruited DCs displaying SIINFEKL-H2K^{b+} on the

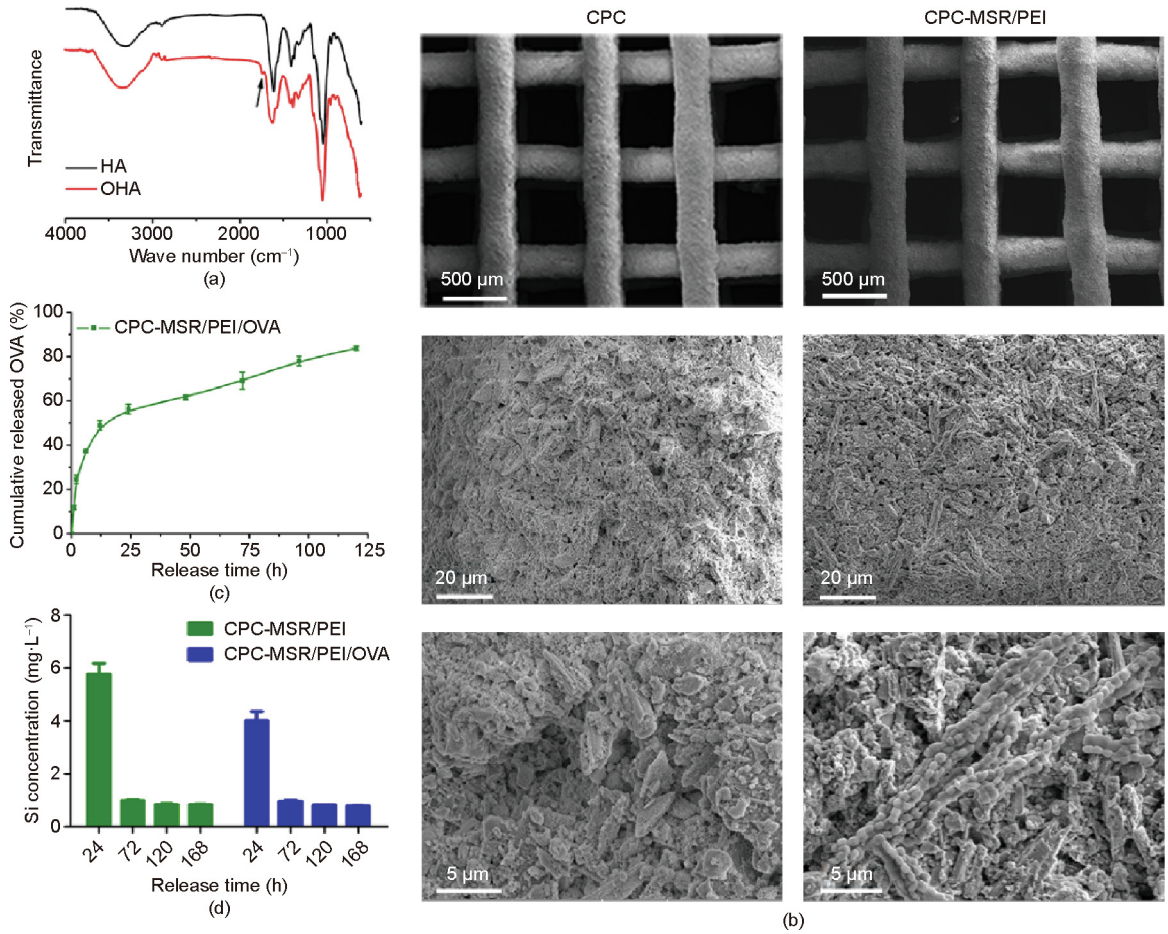

Fig. 3. Characterization of MSR vaccine-loaded scaffolds. (a) FTIR spectra of HA and OHA. (b) SEM images of CPC and MSR/PEI-loaded CPC scaffolds. (c) Cumulative release of OVA from CPC-MSR/PEI/OVA scaffolds. (d) Si ion concentration in the releasing medium.

scaffolds and in their medium, compared with the other two groups. Moreover, the larger number of activated cells in the culture medium of the MSR/PEI/OVA-loaded scaffolds indicated that the antigen released from the scaffolds maintained its function.

3.3. Vaccine-loaded scaffolds promote mBMSC attachment and osteogenesis differentiation

The effects of scaffolds on BMSC viability, attachment, and osteogenic differentiation are vital to bone repair. Previously, we discovered that an appropriate concentration of released Si ions from 3D-printed scaffolds promoted the osteogenic differentiation of BMSCs [37]. However, the biocompatibility and osteogenesis properties of the novel vaccine system remained unknown. Hence, the effect of vaccine loading on mBMSC functions was assayed. The cell viability was detected with a CCK-8 kit (Fig. 5(a)). During the culture period, the mBMSCs in all the groups maintained high viability. According to the SEM observation (Fig. 5(b)), the mBMSCs attached closely onto the scaffolds, with more cells being seen on the CPC-MSR/PEI and CPC-MSR/PEI/OVA scaffolds than on the CPC scaffolds. In addition, the mBMSCs exhibited a more extended morphology on the printed filaments of the CPC-MSR/PEI and MS-MSR/PEI/OVA scaffolds than on the CPC scaffolds. Since the three scaffold groups exhibited similar surface morphologies, the improved cell attachment and spreading was attributed to the positive charge of the MSR/PEIs and MSR/PEI/OVAs. Afterward, the effect of vaccine loading on BMSC osteogenic differentiation was monitored. The ALP activity of the mBMSCs was assessed after culturing with the scaffolds for 7 days. As shown in Fig. 5(c), the ALP-positive areas on the CPC-MSR/PEI and CPC-MSR/PEI/OVA scaffolds were larger than those on the CPC scaffolds, which demonstrated the osteogenesis-promotion property of the vaccine system. The CPC-MSR/PEI scaffolds exhibited a larger ALP-positive area than the CPC-MSR/PEI/OVA scaffolds. This finding is partly attributable to the release of the MSR/PEI/OVA. It is easier for the MSR/PEI/OVA microrods to release from the scaffolds in comparison with the MSR/PEIs because the loading of OVA results in there being fewer available NH_2 groups of PEI to combine with the aldehyde groups on the scaffolds. We also observed more ALP-positive cells in the bottom of the culture well of the CPC-MSR/PEI/OVA scaffolds than in that of the CPC-MSR/PEI scaffolds. Although an ALP-positive area was barely seen on the CPC scaffolds, some of the cells in the bottom of the culture well displayed ALP activity, which is consistent with a previous report [48] and with the cell attachment results. The releasing component of the CPC scaffolds slightly promoted the osteogenic differentiation of BMSCs, while fewer cells attached onto the scaffolds. Moreover, the PCR results (Fig. 5(d)) confirmed the promotion effect of the vaccine system on BMSC osteogenic differentiation. The osteogenic differentiation-related gene expressions of the cells in the

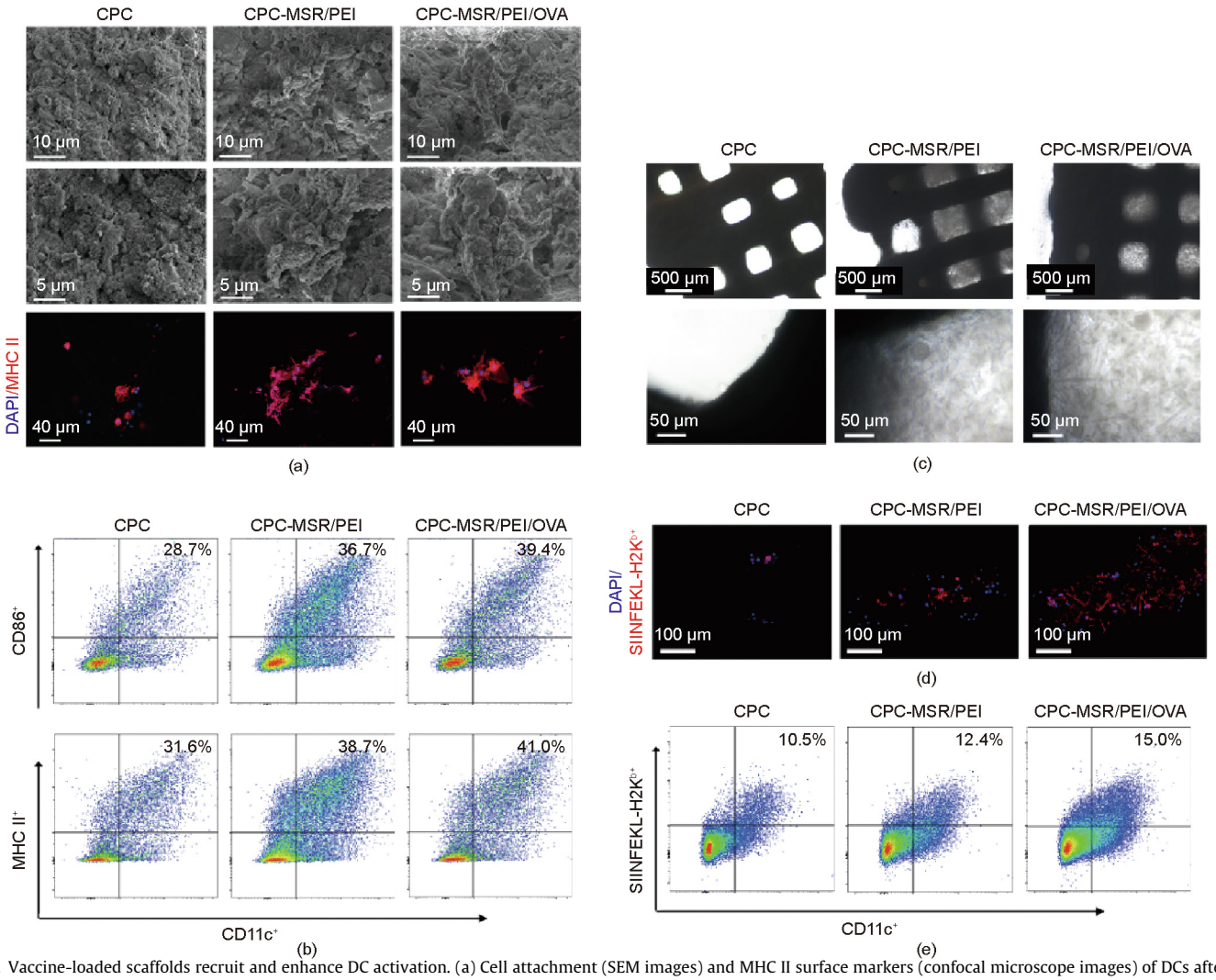

Fig. 4. Vaccine-loaded scaffolds recruit and enhance DC activation. (a) Cell attachment (SEM images) and MHC II surface markers (confocal microscope images) of DCs after 24 h of co-culture with the CPC, CPC-MSR/PEI, and CPC-MSR/PEI/OVA scaffolds. (b) Flow cytometry analysis of CD86 and MHC II expression on DCs after 24 h of co-culture with the CPC, CPC-MSR/PEI, and CPC-MSR/PEI/OVA scaffolds. (c) Cell recruitment in the CPC, CPC-MSR/PEI, and CPC-MSR/PEI/OVA scaffolds after 48 h of co-culture. (d) SIINFEKL-H2K^b surface markers of DCs attached onto the scaffolds (confocal microscope images). (e) Flow cytometry analysis of SIINFEKL-H2K^b expression of DCs in the culture medium after 48 h of co-culture.

CPC-MSR/PEI and CPC-MSR/PEI/OVA scaffolds were much higher than those in the CPC scaffolds. Although the expressions in the CPC-MSR/PEI/OVA scaffolds were lower than those in the CPC-MSR/PEI scaffolds, no statistical difference was detected. Overall, our results demonstrated that the vaccine-system-loaded scaffolds successfully promoted the attachment and osteogenic differentiation of BMSCs. To assess the combination of vaccines and CPC scaffolds, the MSR/PEI- and MSR/PEI/OVA-loaded scaffolds were immersed and rinsed with the culture medium for several days prior to performing the assays. The results above further demonstrated the stable combination.

3.4. Vaccine-loaded scaffolds induce Th2 response and enhance angiogenesis in the subcutaneous embedding model

The ability of MSR/PEI/OVA-loaded scaffolds to generate and recruit CD4$^+$ T cells when subcutaneously implanted with was tested in C57BL/6J mice (Fig. 6(a)). A total of 24 mice were divided into four groups: ① untreated, ② CPC scaffold, ③ CPC-MSR/PEI scaffold, and ④ CPC-MSR/PEI/OVA scaffold. To analyze the Th1 and Th2 responses elicited by the scaffolds, we isolated the spleen CD4$^+$ T cells after 7 days of implantation and assayed the proportion of cells expressing key Th1 and Th2 markers—that is, IFN-γ^+ and IL-4$^+$, respectively (Fig. 6(b)). The CPC-MSR/PEI group showed a higher ratio of both IFN-γ^+ and IL-4$^+$ cells than the untreated and CPC groups, indicating that the MSR/PEIs were able to trigger both Th1 and Th2 responses, which is consistent with a previous report [38]. However, the CPC-MSR/PEI/OVA scaffolds resulted in the production of fewer IFN-γ^+ cells and many more IL-4$^+$ cells than the CPC-MSR/PEI scaffolds ($P < 0.001$). It was found that the CPC-MSR/PEI/OVA scaffolds induced a strong antigen-specific immune reaction with the loading of OVA. Subsequently, the ability of the CPC-MSR/PEI/OVA scaffolds to recruit antigen-specific T cells was tested. After 7 days of implantation, significantly more CD4$^+$ T cells were recruited into the macropores of the CPC-MSR/PEI/OVA scaffolds than into those of the CPC-MSR/PEI and blank scaffolds ($P < 0.001$) (Fig. 6(c)); furthermore, more CD4$^+$ T cells were found in the CPC-MSR/PEI scaffolds than in the blank scaffolds. This trend is consistent with the DC activation results *in vitro*.

It was previously reported that CD4$^+$ T cells recruited by the OVA vaccine efficiently enhanced blood perfusion in hindlimb ischemia [36]. The ability of CPC-MSR/PEI/OVA scaffolds to

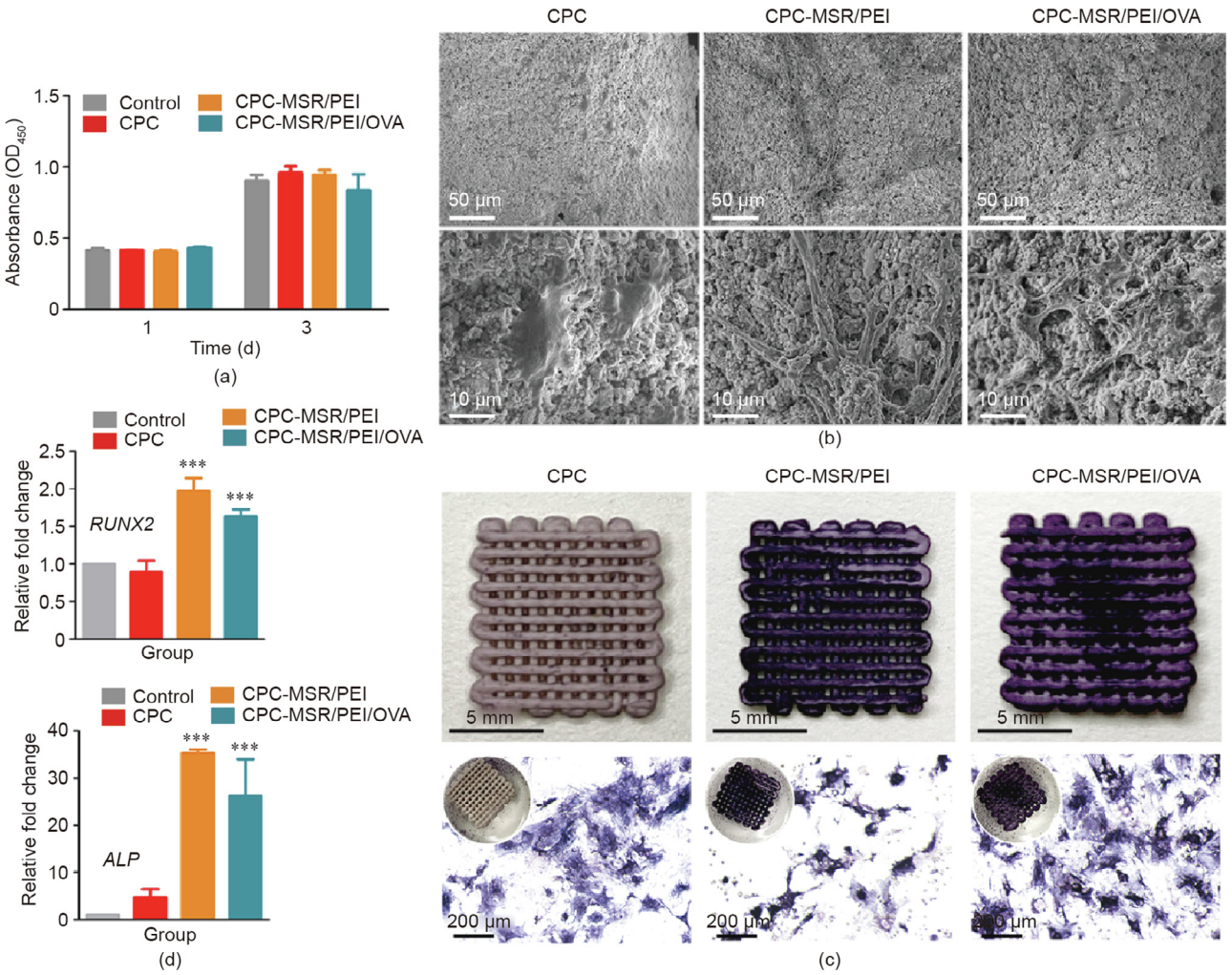

Fig. 5. Vaccine-loaded scaffolds promote the attachment and osteogenic differentiation of mBMSCs. (a) Viability of mBMSCs in the extraction medium of CPC, CPC-MSR/PEI, and CPC-MSR/PEI/OVA scaffolds during 1 and 3 days of culture. (b) SEM images of cell attachment on CPC, CPC-MSR/PEI, and CPC-MSR/PEI/OVA scaffolds. (c) ALP staining of mBMSCs after 7 days of co-culture with CPC, CPC-MSR/PEI, and CPC-MSR/PEI/OVA scaffolds. (d) Expression levels of osteogenic differentiation-related genes *RUNX2* and *ALP* in mBMSCs after 14 days of co-culture in the extraction medium of CPC, CPC-MSR/PEI, and CPC-MSR/PEI/OVA scaffolds. ***$P < 0.001$ vs control. OD_{450}: absorbance at 450 nm.

promote angiogenesis in vaccinated mice was then examined. At day 14 after implantation, blood perfusion inside the scaffolds was assayed using a multimode ultrasound imaging system while the animals were alive (Fig. 6(d)). Since no vascular rupture occurred during the procedure, the blood flow morphology was regarded as the morphology of newly formed blood vessels. It was observed that blood signals flowed through the macropores of the CPC-MSR/PEI/OVA scaffolds from top to bottom, indicating blood vessel formation throughout the scaffolds. Most of the signals were detected on the surface of the CPC scaffolds, while only a few were detected from the top to the middle of the CPC-MSR/PEI scaffolds. Visual inspection of the scaffolds collected from the sacrificed animals (Fig. 6(e)) showed more newly formed blood vessels around and in the CPC-MSR/PEI/OVA scaffolds than in the other scaffolds; moreover, more vessels were observed in the CPC-MSR/PEI scaffolds than in the CPC scaffolds. We further analyzed the $CD31^+$ cells in the scaffolds at 7 and 14 days after implantation (Fig. 6(f)). After 7 days of implantation, more $CD31^+$ cells were observed in the CPC-MSR/PEI and CPC-MSR/PEI/OVA scaffolds than in the CPC scaffolds (Fig. S1 in Appendix A) ($P < 0.001$). After 14 days of implantation, the OVA-releasing scaffold group exhibited many more $CD31^+$ cells, which accumulated and formed the tube morphology of the blood vessels inside the macropores, in comparison with the other two groups (Fig. S1) ($P < 0.001$). Thus, it was confirmed that the vaccine microenvironment swiftly promoted the ingrowth of newly formed blood vessels after scaffold implantation. According to previous reports, IL-5 and IL-10 secreted by antigen-specific T cells in the microenvironment are supposed to directly promote the sprouting of endothelial cells, thereby enhancing angiogenesis [34]. A comprehensive investigation will be performed in our follow-up study. Although an appropriate concentration of released Si ions can promote angiogenesis, OVA-specific immunoreaction was demonstrated to be more efficient in terms of the enhancement effect.

3.5. Vaccine-loaded scaffolds enhance vascularized bone regeneration in a rat skull defect-repair model

Vascularity is a crucial organ for nutrient diffusion, metabolic wastes removal, and signaling molecules regulation in the process of bone regeneration [6,49]. Early vascularization in scaffolds is known to be a prerequisite for osteogenesis [50]. Thus, the effect

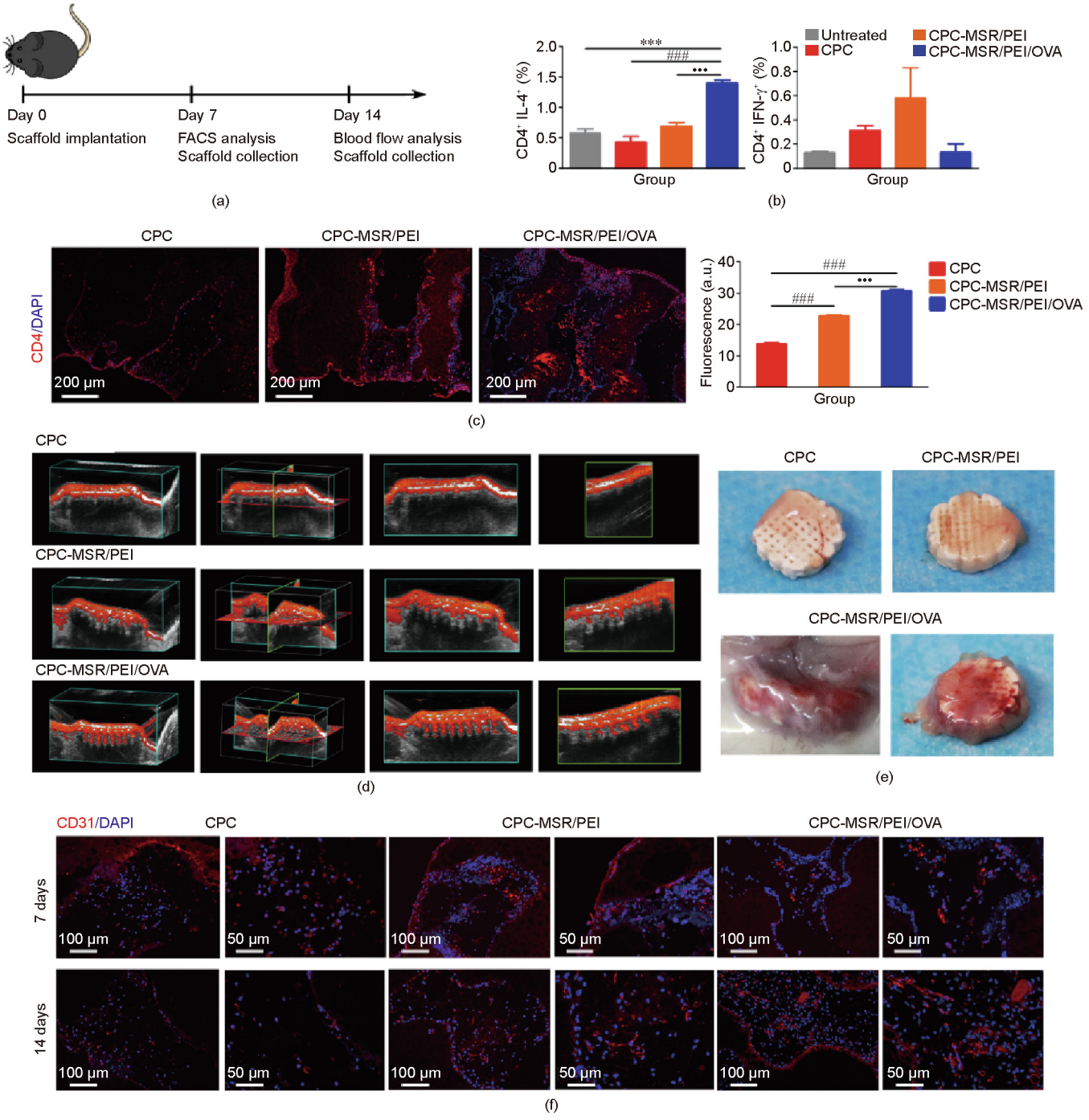

Fig. 6. Vaccine-loaded scaffolds promote antigen-specific cell recruitment and angiogenesis. (a) Schematic representations of the subcutaneous implantation experiment. (b) Ratio of IL-4$^+$ and IFN-γ$^+$ cells among the spleen CD4$^+$ T cells. (c) CD4 immunofluorescence staining images and related fluorescence intensity of implanted scaffolds after 7 days of implantation. (d) Ultrasound images and (e) digital photographs of implanted scaffolds after 14 days of implantation. (f) CD31 immunofluorescence staining images of implanted scaffolds after 7 and 14 days of implantation. $^{***}P < 0.001$ vs control, $^{\#\#\#}P < 0.001$ vs CPC group, $^{\bullet\bullet\bullet}P < 0.001$ vs CPC-MSR/PEI group. FACS analysis: flow cytometry analysis.

of the vaccine-loaded scaffolds on vascularized bone regeneration was analyzed in a rat skull defect-repair model (Fig. 7(a)). According to the micro-CT results (Figs. 7(b) and (c)), the volume ratios of new bones formed in the defects after 8 weeks of implantation in the untreated, CPC, CPC-MSR/PEI, and CPC-MSR/PEI/OVA groups were (5.02 ± 0.35)%, (8.78 ± 0.61)%, (11.13 ± 2.45)%, and (12.18 ± 0.39)%, respectively. The CPC-MSR/PEI/OVA group demonstrated the best bone-repair effect, with the highest bone volume to total volume ratio (BV/TV) ($P < 0.01$). As seen from the 3D reconstructed images, more newly formed bones were observed around and inside the CPC-MSR/PEI/OVA scaffolds than in the other groups. In addition, the CPC-MSR/PEI scaffolds showed a better osteogenesis-promotion effect than the CPC scaffolds. Afterward, histological analysis of osteogenesis and angiogenesis in

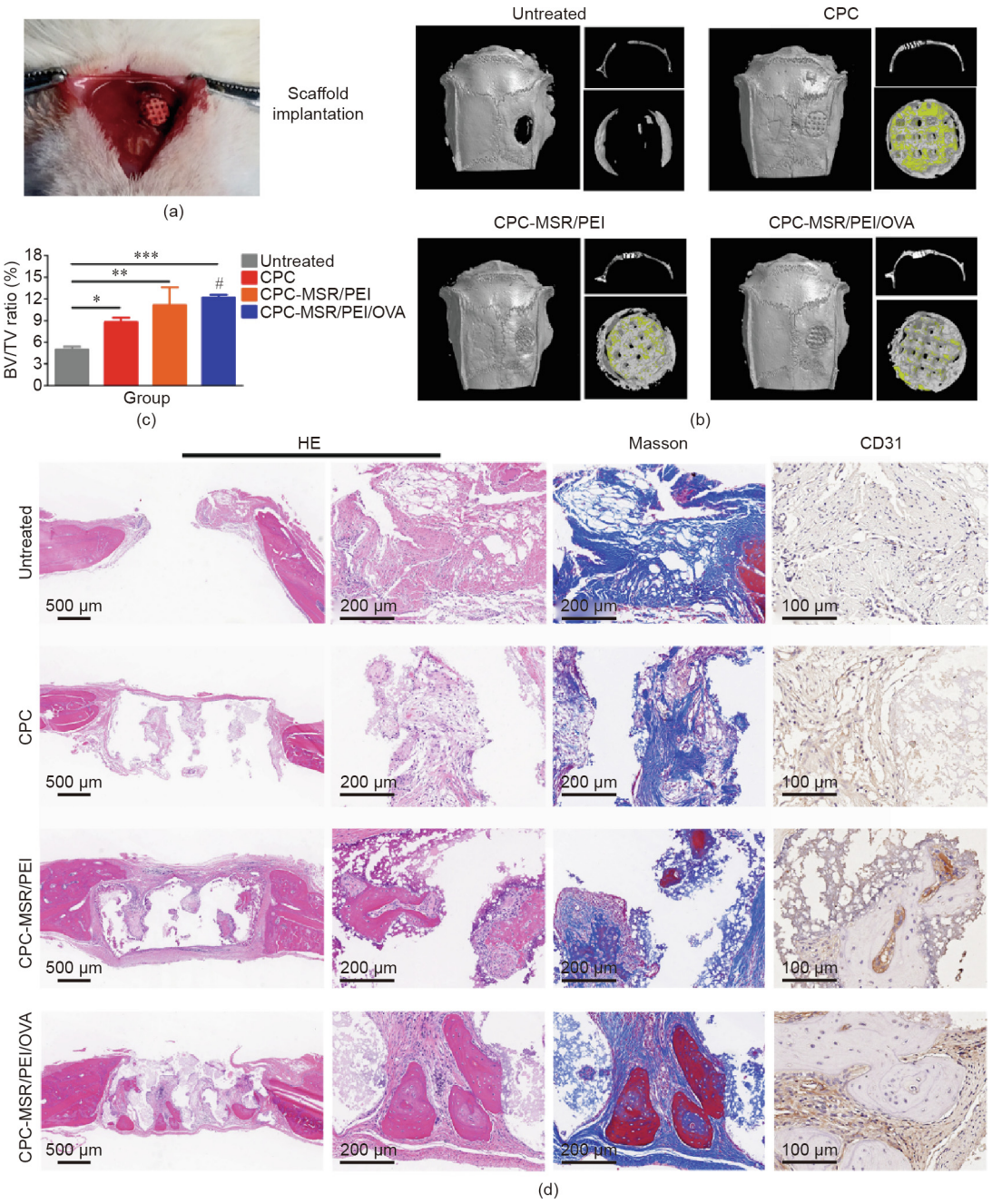

Fig. 7. Vaccine-loaded scaffolds promote vascularized bone regeneration in rat skull defect. (a) Photograph of the scaffold implantation in rat skull defect. (b) Micro-CT images after 8 weeks of implantation: 3D-reconstructed images of the skulls implanted with scaffolds, transverse-view images of the skulls with scaffolds, and images of reconstructed scaffolds with newly formed bones (white for newly formed bone and yellow for scaffolds). (c) Volume ratio of the newly formed bone to defects (bone volume to total volume ratio (BV/TV)) of all groups (n = 3). (d) HE staining, Masson staining, and CD31 immunohistochemical staining of implanted scaffolds. $^{*}P < 0.05$, $^{**}P < 0.01$, $^{***}P < 0.001$ vs untreated group; $^{\#}P < 0.05$ vs CPC group.

the defects was performed. According to the HE and Masson staining results (Fig. 7(d)), more mature bones were regenerated in the CPC-MSR/PEI/OVA scaffolds than in the CPC-MSR/PEI scaffolds. Newly formed bones were barely observed in the untreated group and CPC scaffolds. Furthermore, abundant $CD31^{+}$ cells aggregating into tubes were observed in the macropores and newly formed bones in the CPC-MSR/PEI and CPC-MSR/PEI/OVA scaffolds.

In this study, the osteogenesis-promotion effect of the CPC-MSR/PEI scaffolds was consistent with our expectation. Since functional Si ion concentration around the CPC-MSR/PEI and CPC-MSR/PEI/OVA scaffolds should be at the same level, the more efficient osteogenesis-promotion effect of the CPC-MSR/PEI/OVA scaffolds was presumed to be closely related to the presence of more blood vessels, which rapidly formed after implantation.

4. Conclusions

Through the stable loading of MSR/PEI/OVA vaccines, 3D-printed scaffolds with an antigen-specific T cell recruitment function were successfully constructed in this study. After the laminar-ordered mesoporous and highly specific surface area structures were verified, the MSRs were assembled layer by layer with the branched cationic polymer PEI and the antigen OVA to prepare MSR/PEI/OVA vaccines rich in amino groups. Based on the Schiff base reaction, the vaccines were covalently cross-linked with the aldehyde groups on the surface of the scaffolds, which led to the gradual release of OVA and Si ions. *In vitro* results showed that the loaded vaccines not only recruited and activated DCs to process the antigen, but also promoted the attachment, spreading, and osteogenic differentiation of BMSCs on the scaffolds. In vaccinated animals, the gradually released OVA efficiently recruited antigen-specific $CD4^+$ T cells, promoted local angiogenesis, and increased perfusion in the scaffolds. With the increased blood supply and released Si ions, osteogenesis was promoted in the MSR/PEI/OVA-loaded scaffolds. Overall, we have developed a therapeutic platform of antigen-specific immunoregulatory 3D-printed scaffolds for angiogenesis promotion.

Acknowledgments

This investigation was supported by the National Key Research and Development Program of China (2019YFA0112000 and 2018YFB1105600), the National Natural Science Foundation of China (81930051), Shanghai Municipal Education Commission—Gaofeng Clinical Medicine Grant Support (20171906), Shanghai Jiao Tong University "Medical and Research" Program (ZH2018ZDA04), and Foundation of National Facility for Translational Medicine (Shanghai) (TMSK-2020-117).

Compliance with ethics guidelines

Cuidi Li, Zhenjiang Ma, Wentao Li, Tianyang Jie, Liping Zhong, Hongfang Chen, Wenhao Wang, Jinwu Wang, Wenguo Cui, and Yongxiang Zhao declare that they have no conflict of interest or financial conflicts to disclose.

Appendix A. Supplementary data

Supplementary data to this article can be found online at https://doi.org/10.1016/j.eng.2021.05.018.

References

[1] Keating JF, Simpson AHRW, Robinson CM. The management of fractures with bone loss. J Bone Joint Surg Br 2005;87-B(2):142–50.
[2] Zhang L, Yang G, Johnson BN, Jia X. Three-dimensional (3D) printed scaffold and material selection for bone repair. Acta Biomater 2019;84:16–33.
[3] Wang H, Su K, Su L, Liang P, Ji P, Wang C. The effect of 3D-printed Ti_6Al_4V scaffolds with various macropore structures on osteointegration and osteogenesis: a biomechanical evaluation. J Mech Behav Biomed Mater 2018;88:488–96.
[4] Du R, Su YX, Yan Y, Choi WS, Yang WF, Zhang C, et al. A systematic approach for making 3D-printed patient-specific implants for craniomaxillofacial reconstruction. Engineering 2020;6(11):1291–301.
[5] Hao Y, Wang L, Jiang W, Wu W, Ai S, Shen Lu, et al. 3D printing hip prostheses offer accurate reconstruction, stable fixation, and functional recovery for revision total hip arthroplasty with complex acetabular bone defect. Engineering 2020;6(11):1285–90.
[6] Wang X, Zhang M, Ma J, Xu M, Chang J, Gelinsky M, et al. 3D printing of cell-container-like scaffolds for multicell tissue engineering. Engineering 2020;6(11):1276–84.
[7] Raisian S, Fallahi HR, Khiabani KS, Heidarizadeh M, Azdoo S. Customized titanium mesh based on the 3D printed model vs. manual intraoperative bending of titanium mesh for reconstructing of orbital bone fracture: a randomized clinical trial. Rev Recent Clin Trials 2017;12(3):154–8.
[8] Laschke MW, Harder Y, Amon M, Martin I, Farhadi J, Ring A, et al. Angiogenesis in tissue engineering: breathing life into constructed tissue substitutes. Tissue Eng 2006;12(8):2093–104.
[9] Rouwkema J, Rivron NC, van Blitterswijk CA. Vascularization in tissue engineering. Trends Biotechnol 2008;26(8):434–41.
[10] Stegen S, van Gastel N, Carmeliet G. Bringing new life to damaged bone: the importance of angiogenesis in bone repair and regeneration. Bone 2015;70:19–27.
[11] Kanczler JM, Oreffo RO. Osteogenesis and angiogenesis: the potential for engineering bone. Eur Cell Mater 2008;15:100–14.
[12] Cao L, Mooney D. Spatiotemporal control over growth factor signaling for therapeutic neovascularization. Adv Drug Deliv Rev 2007;59(13):1340–50.
[13] Fahimipour F, Rasoulianboroujeni M, Dashtimoghadam E, Khoshroo K, Tahriri M, Bastami F, et al. 3D printed TCP-based scaffold incorporating VEGF-loaded PLGA microspheres for craniofacial tissue engineering. Dent Mater 2017;33(11):1205–16.
[14] Place ES, Evans ND, Stevens MM. Complexity in biomaterials for tissue engineering. Nat Mater 2009;8(6):457–70.
[15] Chen RR, Snow JK, Palmer JP, Lin AS, Duvall CL, Guldberg RE, et al. Host immune competence and local ischemia affects the functionality of engineered vasculature. Microcirculation 2007;14(2):77–88.
[16] Li T, Peng M, Yang Z, Zhou X, Deng Y, Jiang C, et al. 3D-printed IFN-γ-loading calcium silicate-β-tricalcium phosphate scaffold sequentially activates M1 and M2 polarization of macrophages to promote vascularization of tissue engineering bone. Acta Biomater 2018;71:96–107.
[17] Sun X, Ma Z, Zhao X, Jin W, Zhang C, Ma J, et al. Three-dimensional bioprinting of multicell-laden scaffolds containing bone morphogenic protein-4 for promoting M2 macrophage polarization and accelerating bone defect repair in diabetes mellitus. Bioact Mater 2021;6(3):757–69.
[18] Niu Y, Wang L, Yu N, Xing P, Wang Z, Zhong Z, et al. An "all-in-one" scaffold targeting macrophages to direct endogenous bone repair *in situ*. Acta Biomater 2020;111:153–69.
[19] Spiller KL, Nassiri S, Witherel CE, Anfang RR, Ng J, Nakazawa KR, et al. Sequential delivery of immunomodulatory cytokines to facilitate the M1-to-M2 transition of macrophages and enhance vascularization of bone scaffolds. Biomaterials 2015;37:194–207.
[20] Roh JD, Sawh-Martinez R, Brennan MP, Jay SM, Devine L, Rao DA, et al. Tissue-engineered vascular grafts transform into mature blood vessels via an inflammation-mediated process of vascular remodeling. Proc Natl Acad Sci USA 2010;107(10):4669–74.
[21] Feng Y, Li Q, Wu D, Niu Y, Yang C, Dong L, et al. A macrophage-activating, injectable hydrogel to sequester endogenous growth factors for *in situ* angiogenesis. Biomaterials 2017;134:128–42.
[22] Spiller KL, Anfang RR, Spiller KJ, Ng J, Nakazawa KR, Daulton JW, et al. The role of macrophage phenotype in vascularization of tissue engineering scaffolds. Biomaterials 2014;35(15):4477–88.
[23] Takeda Y, Costa S, Delamarre E, Roncal C, Leite de Oliveira R, Squadrito ML, et al. Macrophage skewing by *Phd2* haplodeficiency prevents ischaemia by inducing arteriogenesis. Nature 2011;479(7371):122–6.
[24] Murray PJ. Macrophage polarization. Annu Rev Physiol 2017;79(1):541–66.
[25] Sica A, Mantovani A. Macrophage plasticity and polarization: *in vivo* veritas. J Clin Invest 2012;122:787–95.
[26] Kong L, Smith W, Hao D. Overview of RAW264.7 for osteoclastogensis study: phenotype and stimuli. J Cell Mol Med 2019;23(5):3077–87.
[27] Eger M, Hiram-Bab S, Liron T, Sterer N, Carmi Y, Kohavi D, et al. Mechanism and prevention of titanium particle-induced inflammation and osteolysis. Front Immunol 2018;9:2963.
[28] Loi F, Córdova LA, Zhang R, Pajarinen J, Lin TH, Goodman SB, et al. The effects of immunomodulation by macrophage subsets on osteogenesis *in vitro*. Stem Cell Res Ther 2016;7:15.
[29] Könnecke I, Serra A, El Khassawna T, Schlundt C, Schell H, Hauser A, et al. T and B cells participate in bone repair by infiltrating the fracture callus in a two-wave fashion. Bone 2014;64:155–65.
[30] Croes M, Öner FC, van Neerven D, Sabir E, Kruyt MC, Blokhuis TJ, et al. Proinflammatory T cells and IL-17 stimulate osteoblast differentiation. Bone 2016;84:262–70.
[31] Grassi F, Cattini L, Gambari L, Manferdini C, Piacentini A, Gabusi E, et al. T cell subsets differently regulate osteogenic differentiation of human mesenchymal stromal cells *in vitro*. J Tissue Eng Regen Med 2016;10(4):305–14.
[32] Stabile E, Burnett MS, Watkins C, Kinnaird T, Bachis A, la Sala A, et al. Impaired arteriogenic response to acute hindlimb ischemia in *CD4*-knockout mice. Circulation 2003;108(2):205–10.
[33] van Weel V, Toes REM, Seghers L, Deckers MML, de Vries MR, Eilers PH, et al. Natural killer cells and $CD4^+$ T-cells modulate collateral artery development. Arterioscler Thromb Vasc Biol 2007;27(11):2310–8.
[34] Kwee BJ, Budina E, Najibi AJ, Mooney DJ. CD4 T-cells regulate angiogenesis and myogenesis. Biomaterials 2018;178:109–21.
[35] Puxeddu I, Alian A, Piliponsky AM, Ribatti D, Panet A, Levi-Schaffer F. Human peripheral blood eosinophils induce angiogenesis. Int J Biochem Cell Biol 2005;37(3):628–36.
[36] Kwee BJ, Seo BR, Najibi AJ, Li AW, Shih TY, White D, et al. Treating ischemia via recruitment of antigen-specific T cells. Sci Adv 2019;5(7):eaav6313.
[37] Li C, Jiang C, Deng Y, Li T, Li N, Peng M, et al. RhBMP-2 loaded 3D-printed mesoporous silica/calcium phosphate cement porous scaffolds with enhanced vascularization and osteogenesis properties. Sci Rep 2017;7(1):41331.

[38] Kim J, Li WA, Choi Y, Lewin SA, Verbeke CS, Dranoff G, et al. Injectable, spontaneously assembling, inorganic scaffolds modulate immune cells *in vivo* and increase vaccine efficacy. Nat Biotechnol 2015;33(1):64–72.
[39] Li L, Wang N, Jin X, Deng R, Nie S, Sun L, et al. Biodegradable and injectable *in situ* cross-linking chitosan-hyaluronic acid based hydrogels for postoperative adhesion prevention. Biomaterials 2014;35(12):3903–17.
[40] Li C, Wang K, Li T, Zhou X, Ma Z, Deng C, et al. Patient-specific scaffolds with a biomimetic gradient environment for articular cartilage-subchondral bone regeneration. ACS Appl Bio Mater 2020;3(8):4820–31.
[41] Zou D, Zhang Z, He J, Zhu S, Wang S, Zhang W, et al. Repairing critical-sized calvarial defects with BMSCs modified by a constitutively active form of hypoxia-inducible factor-1α and a phosphate cement scaffold. Biomaterials 2011;32(36):9707–18.
[42] Li AW, Sobral MC, Badrinath S, Choi Y, Graveline A, Stafford AG, et al. A facile approach to enhance antigen response for personalized cancer vaccination. Nat Mater 2018;17(6):528–34.
[43] St John AL, Chan CY, Staats HF, Leong KW, Abraham SN. Synthetic mast-cell granules as adjuvants to promote and polarize immunity in lymph nodes. Nat Mater 2012;11(3):250–7.
[44] Moon JJ, Suh H, Li AV, Ockenhouse CF, Yadava A, Irvine DJ. Enhancing humoral responses to a malaria antigen with nanoparticle vaccines that expand Tfh cells and promote germinal center induction. Proc Natl Acad Sci USA 2012;109(4):1080–5.
[45] Hammer GE, Ma A. Molecular control of steady-state dendritic cell maturation and immune homeostasis. Annu Rev Immunol 2013;31:743–91.
[46] Banchereau J, Steinman RM. Dendritic cells and the control of immunity. Nature 1998;392(6673):245–52.
[47] Nguyen TL, Choi Y, Kim J. Mesoporous silica as a versatile platform for cancer immunotherapy. Adv Mater 2019;31(34):1803953.
[48] Zhang J, Zhou H, Yang K, Yuan Y, Liu C. RhBMP-2-loaded calcium silicate/calcium phosphate cement scaffold with hierarchically porous structure for enhanced bone tissue regeneration. Biomaterials 2013;34(37):9381–92.
[49] Yan Y, Chen H, Zhang H, Guo C, Yang K, Chen K, et al. Vascularized 3D printed scaffolds for promoting bone regeneration. Biomaterials 2019;190–191:97–110.
[50] Wang Z, Wang Y, Yan J, Zhang K, Lin F, Xiang L, et al. Pharmaceutical electrospinning and 3D printing scaffold design for bone regeneration. Adv Drug Deliver Rev 2021;174:504–34.